

13. Mazets E P et al. *Astrophys. J.* **680** 545 (2008)
14. Aptekar R L et al. *Astrophys. J. Lett.* **698** L82 (2009)
15. Van der Horst A J et al. *Astrophys. J. Lett.* **711** L1 (2010)
16. Racusin J L et al. *Nature* **455** 183 (2008)
17. Aptekar R L et al. *Astrophys. J. Suppl.* **137** 227 (2001)

PACS numbers: 95.55.Ka, 95.85.Pw, 98.70.Rz
DOI: 10.3367/UFNe.0180.201004h.0424

Discovery of the fast optical variability of GRB 080319B and the prospects for wide-field optical monitoring with high time resolution

G M Beskin, S V Karpov, S V Bondar,
V L Plokhotnichenko, A Guarnieri,
C Bartolini, G Greco, A Piccioni

1. Introduction

The systematic investigation of the night sky variability on a subsecond time scale is an important but still largely unaddressed issue. That the observations of this kind are necessary for the search for transient objects with a priori unknown localization and for their study was already emphasized by Bondi [1]. Investigations have been pursued in this area [2, 3]; but owing to technical difficulties, they either were able to attain a high temporal resolution on the level of several dozen microseconds in monitoring $5' - 10'$ fields or used a temporal resolution of 5–10 s for wide ($20^\circ - 30^\circ$) fields. The currently operating wide-field monitoring systems, like WIDGET [4], RAPTOR [5], BOOTES [6], and ‘Pi of the Sky’ [7], have large fields of view with relatively good detection limits, but low temporal resolution, which hinders their use for detecting fast transients.

We give several examples of these transients: UV Cet-type stellar flares with rise times 0.2–0.5 s [8], 30% of gamma-ray bursts that last less than 2 s, while individual details of their light curves may be as short as 1 ms [9]. Also of substantial interest are very fast meteors, which are conceivably produced beyond the Solar System [10].

One further problem that invites conducting regular wide-field observations with a high temporal resolution is the monitoring of circumterrestrial space. The trajectories of a large number of satellites, as well as of a great quantity of small particles of space debris, change rather quickly and the speeds of these objects are quite high, making their observation by conventional techniques a very difficult task.

Since the late 1990s, we are developing the strategy of optical monitoring with a high temporal resolution of celestial

sphere regions comparable in size to the field of view of spaceborne gamma-ray telescopes. Initially, we planned to use instruments with large mirrors of relatively low quality [11, 12], for instance, Cherenkov telescopes and solar concentrators involving photomultiplier arrays with a temporal resolution as high as several microseconds. But more recently, we decided in favor of a project involving a wide-field camera with a lens of a relatively small diameter, an image intensifier (II) for the effective shortening of the focal length, and a fast low-noise CCD (charge-coupled device). A prototype of this system, FAVOR (FAst Variability Optical Registrator), put into operation in 2003, is located near the 6-meter BTA (Big Telescope Alt-azimuthal) of the Special Astrophysical Observatory of the Russian Academy of Sciences [13, 14]. The TORTORA (Telescopio Ottimizzato per la Ricerca dei Transienti Ottici RAPidi) camera of similar design [15], which was installed on the mounting of the Rapid Eye Mount (REM) robotic telescope in the La Silla Observatory (ESO, European Southern Observatory, Chile) in 2006, makes up a two-telescope TORTOREM complex together with REM [17]. It was precisely this camera that discovered and enabled a detailed study of the optical emission of the brightest ever gamma-ray burst GRB 080319B [18–20].

In this report, we describe the design and special implementation features of the TORTORA camera and outline several results of its operation, including a comprehensive analysis of the data on the GRB 080319B burst. Also discussed is the project of a next-generation wide-field monitoring system capable not only of discovering much weaker transients but also of performing their multicolor photometry and polarimetry.

2. Description of the wide-field cameras FAVOR and TORTORA

The parameters of the FAVOR and TORTORA cameras are compared with those of other presently existing wide-field monitoring systems in Table 1. It follows that only the FAVOR and TORTORA cameras have a high temporal resolution and a relatively large field of view.

The structure of the TORTORA camera is diagrammed in Fig. 1, its parameters are collected in Table 2, and its image is given in Fig. 2. The instrument consists of the main

Table 1. Main optical wide-field monitoring systems currently operating.

Designation	Field of view, deg	Resolution, s	Detection threshold
WIDGET	62×62	5	10^m
RAPTOR A/B	40×40	60	12^m
RAPTOR Q	180×180	10	10^m
BOOTES	16×11	30	12^m
BOOTES-AllSky	180×180	30	10^m
‘Pi of the Sky’	33×33	10	11.5^m
AROMA-W	25×35	5–100	$10.5^m - 13^m$
MASTER-VWF	20×21	5	11.5^m
MASTER-Net	30×30	1	9^m
FAVOR*	16×24	0.13	$10^m - 11.5^m$
TORTORA*	24×32	0.13	$9^m - 10.5^m$

* For the FAVOR and TORTORA cameras, the detection threshold corresponds to the detection of a transient at a 3σ level in a single frame and may be different from the real detection threshold of the difference technique being used.

G M Beskin, S V Karpov, V L Plokhotnichenko Special Astrophysical Observatory, Russian Academy of Sciences, Nizhnii Arkhyz, Karachaevo-Cherkessiya, Russian Federation. E-mail: beskin@sao.ru

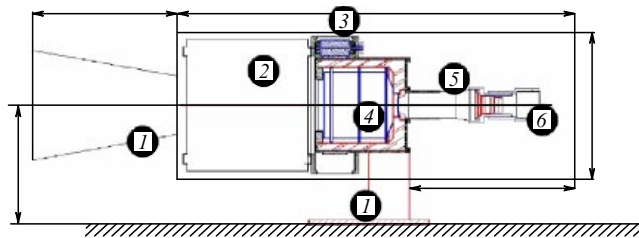
S V Bondar Scientific Research Institute of Precision Instrument Making, Moscow, Russian Federation

A Guarnieri, C Bartolini, A Piccioni Astronomy Department, Bologna University, Bologna, Italy

G Greco Astronomical Observatory of Bologna, INAF, Italy

Table 2. Technical parameters of the TORTORA camera.

Main objective		Image intensifier		CCD matrix	
Diameter	120 mm	Photocathode	S20	Model	VS-CTT285-2001
Focal length	150 mm	Diameter	90 mm	Size	1388 × 1036 pixels
D/F	1/1.2	Gain	150	Scale	81"/pixel
Field of view	24 × 32 deg	Scaling	7.7	Exposure time	0.13–10 s
		Quantum efficiency	10%	Pixel size	6.45 μm

**Figure 1.** Schematic diagram of the TORTORA camera: 1—viewing hood, 2—main objective, 3—main objective focusing unit, 4—image intensifier, 5—image-transfer optics and CCD-matrix focusing unit, 6—fast CCD matrix.**Figure 2.** Image of the TORTORA camera mounted on the REM robotic telescope in the La Silla Observatory (ESO, Chile).

objective 2, its focusing unit 3, an image intensifier 4 used for scaling and intensifying images, image-transfer optics 5, and a fast low-noise CCD matrix 6. The camera is mounted on a robotic REM telescope with an alt-azimuthal mount.

The fast CCD matrix records 7.5 frames per second for the exposure time 0.128 s; in this case, the intervals between individual exposures are negligible. The information from the matrix is distributed via a gigabit local area network and is stored in a 1 terabyte RAID disk array. The data stream is equal to about 20 Mb s⁻¹, and therefore the information obtained during one night of observations may be stored for only one day. Apart from that, the data are transferred to a dedicated computer for real-time processing with the aid of special-purpose software controlled by the Linux operating system. Various kinds of transient objects are detected and classified, and previously known objects are eliminated by comparing their related information with the data from satellite and stellar catalogues.

3. The method of detecting transients

Wide-field monitoring cameras with high temporal resolution can be used for the detection and investigation of different classes of transient events (variable stars, supernovae, active galactic nuclei, microlensing events, occultation of stars by planets) with constant, although a priori unknown coordinates. On the other hand, FAVOR- and TORTORA-type cameras are also able to track moving objects: artificial satellites, elements of space debris, comets, asteroids, and meteors. Special-purpose algorithms of data processing were elaborated for addressing these issues.

Because of the high intensity of the observational information data stream, it is hardly possible to use standard photometric packages for real-time information processing, and we therefore developed a special fast method for extracting transients. This method is based on studying the statistical behavior of the radiation intensity I in every image pixel in the course of time. The instantaneous value of I is compared with the current average

$$\langle I \rangle = \sum \frac{I}{N}, \quad (1)$$

which is evaluated for some number (e.g., $N = 100$, which corresponds to a temporal window of 13 s) of preceding frames, and with the sample variance

$$\sigma_I = \sqrt{\frac{\sum I^2 - (\sum I)^2 / N}{N - 1}} \quad (2)$$

to determine the significance of its deviation from the average

$$A = \frac{I - \langle I \rangle}{\sigma_I}. \quad (3)$$

All pixels with a high significance are then grouped into spatially connected clusters—observable objects. Some of them, e.g., single-pixel events, are rejected as noise.

When all objects in a given frame are revealed, their positions are compared with the trajectories of previously revealed transients (all objects are assumed to be moving, immobile objects are considered to be moving with zero velocity). The detection of an object in three sequential frames (on a temporal scale of 0.4 s) is sufficient for making an assertion that the object belongs to one of three possible classes: ‘noise’ events if the object disappears after a single frame, moving objects if it displays a statistically significant position variation, or immobile transients. The flare events of slowly moving high-altitude artificial satellites are identified by comparing the positions of the transients with the data from regularly updated catalogues of orbital satellite elements [21].

Revealing meteors, however, requires a somewhat different approach, because they are typically seen only in one or two frames. Furthermore, their velocities are substantially higher than those of artificial satellites. Events of this kind are distinguished by their high brightness and length.

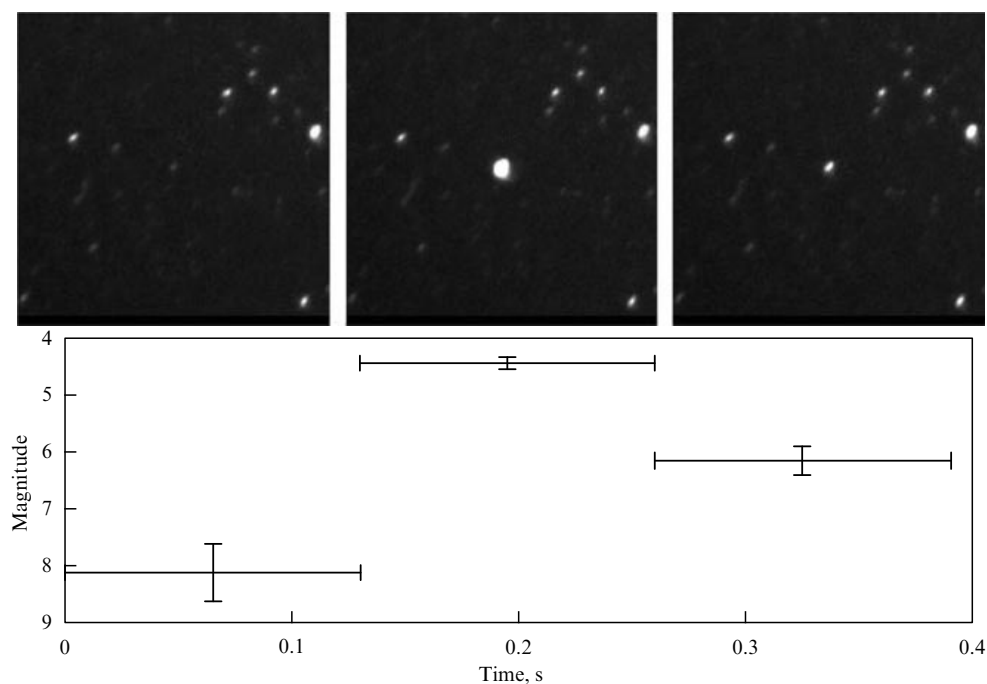


Figure 3. Example of a short flare (result of high-altitude satellite rotation) detected by the monitoring camera. The total duration of the event is 0.4 s; it is observed in three sequential frames.

Astrometric and photometric calibration is regularly performed (once a minute for the TORTORA camera, because the alt-azimuthal mount leads to a systematic rotation of the field of view) via a special procedure involving photometric measurements of all stars in a frame with the help of the SExtractor code [22] and their identification in the *Tycho-2* astrometric catalogue [23].

Therefore, the real-time data analysis system enables detecting and classifying any sufficiently bright optical transients 0.4 s after their emergence and up to the instant their brightness becomes lower than the difference method detection level. A rather short flare of this kind is exemplified in Fig. 3. Upon detection and classification, the information about an event can be transferred to the network for conducting an in-depth investigation. Furthermore, all real-time data about the transient, including its light curve, trajectory, and images of its neighborhood, may be stored for further studies.

4. Results obtained by the TORTORA camera

About half of the available observation time (when the REM telescope does not conduct routine observations), the TORTORA wide-field monitoring camera, which has been in service since June 2006, monitors celestial sphere regions observed at the moment by the Swift spacecraft, in accordance with the telemetric information distributed in real time through the GCN (Gamma-Ray Burst Coordination Network) [24].

Every observation night, the camera detects about 300 meteors and 150 transits of satellites with varying brightnesses.

4.1 Gamma-ray burst observations in the reactive regime
Owing to the automatic reaction of the REM telescope to reports of gamma-ray burst detection by spacecraft, the TORTORA camera has been able to observe the

Table 3. Upper limits of the constant component of the optical flux and of the sinusoidal variable component of the brightness of possible optical transients.

Flare	Beginning of observations (Time since event), s	13 s limit (100 frames)	Frequency range, Hz	Upper limit
GRB060719	59	12.4	0.01 – 3.5	15.3 ^m
GRB061202	92	11.3	0.1 – 3.5	14.0 ^m
GRB060719	118	11.3	0.01 – 3.5	16.4 ^m

error boxes of three gamma-ray bursts shortly after their onset [25–27].

The upper limits for the brightness of the corresponding optical transients obtained in these observations are collected in Table 3. The limits for the constant component of the flux were obtained by analyzing 100 sequential frames, which corresponds to the effective temporal resolution of 12.8 s.

4.2 GRB080319B gamma-ray burst observations

The 19th and 20th of March 2008 turned out to be most fruitful for wide-field monitoring systems all over the world. At that time, five gamma-ray bursts were recorded during 24 hours. One of the bursts, GRB080319B [28], was the brightest of all those observed in the gamma-ray range, as well as in the optical range, and was the first to be independently discovered by a ground-based monitoring system. Its position on the celestial sphere was observed by the Pi of the Sky [29], RAPTOR Q [30], and TORTORA [18] cameras prior to, during, and after the gamma-ray event.

Our TORTORA camera monitored the position of the GRB 080319B burst [18, 19] from 05:46:22 UT, approximately half an hour prior to its onset (the time of its discovery in the gamma-ray range: 06:12:49 UT), as well as during several dozen minutes after its termination. In the interval between 06:13:13 and 06:13:20 UT, the REM robotic telescope performed an automatic repointing on receiving

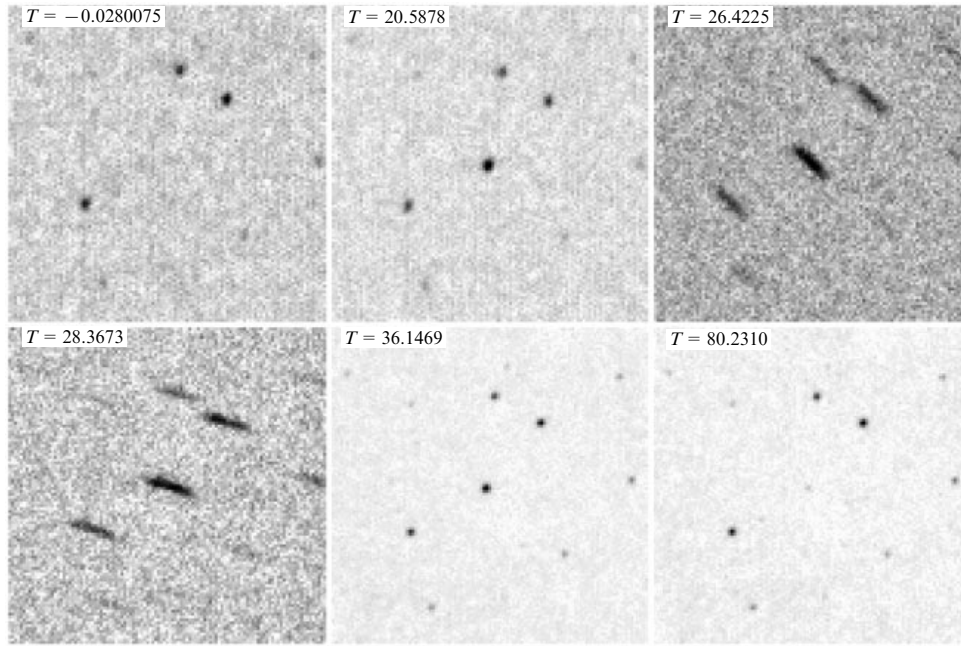


Figure 4. Images of the optical transient arising from the GRB 080319B gamma-ray burst as seen by the TORTORA camera at different stages of its development. Shown are the sums of 10 consecutive frames with the effective temporal resolution of 1.3 s for the onset of the gamma-ray event ($T \approx 0$), the instant of the highest brightness of the first peak ($T \approx 20.6$ s), two points in about the middle of the event ($T \approx 26.4$ s and $T \approx 28.4$ s), during the last peak ($T \approx 36$ s), and at the stage of early afterglow ($T \approx 80$ s). The field size is 2.5 by 2.5 degrees. The stellar profiles in the third and fourth frames were deformed in the course of repointing (from $T \approx 24$ s to $T \approx 31$ s) of the REM robotic telescope on which the camera was mounted, using the burst coordinates obtained from the Swift space telescope. Initially, the burst was located at the edge of the camera field of view; due to the repointing, it shifted to the center of the field of view, resulting in some improvement in the quality of the images.

the coordinates distributed by the Swift satellite [28], which moved the position of the burst from the edge of the camera field of view to its center. Figure 4 shows sample images of the burst region at different stages of the event.

The images acquired by the camera were processed using a conventional reduction procedure involving CCD-matrix noise reduction and flat-fielding. Flux measurements were made with the use of a custom version of the aperture photometry technique and the DAOPHOT code of the IRAF (Image Reduction and Analysis Facility) package for the entire dataset, with the exception of the repointing interval. At this phase, the images of the object and the neighboring stars were deformed because of their significant displacement during the exposure time, which substantially decreased the signal-to-noise ratio. As a result, the flux could not be accurately measured in individual frames. We summed nonoverlapping sequences of 10 frames with the corresponding shift to compensate stellar motion. For the track images thus obtained, the signal-to-noise ratio is in reasonable agreement with that in the remaining portions of the light curve (Fig. 5b). Next, from the summary frames, we measured the fluxes arising from the object and the neighboring stars, using aperture photometry with elliptic apertures and the method of the point scattering function approximation. Both techniques yielded mutually consistent results. We made a separate check of the behavior of the fluxes from comparison stars and found no features that might cast doubt on the accuracy of photometry and brightness variability for the object in the given interval. The effective temporal resolution was 1.3 s in this case; for all other phases of the flare, the photometry was performed with both high (0.13 s, individual frames) and low (1.3 s, sums of 10 consecutive images) temporal resolution. The

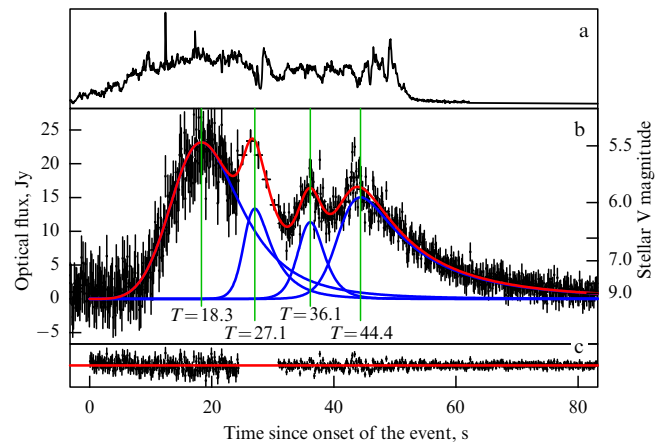


Figure 5. Light curve of the optical companion of the GRB 080319B gamma-ray burst, according to the data obtained from the wide-field TORTORA camera. (a) Gamma-ray radiation, which commences at the instant $T \approx -4$ s and decays at $T \approx 55$ s. (b) High-temporal-resolution data (0.13 s exposure, shown in gray) are available for the entire gamma-ray activity period except the interval of REM telescope repointing ($24.5 \text{ s} < T < 31 \text{ s}$); low-resolution data obtained with the effective exposure time 13 s by summation of each 10 consecutive frames, available for the entire duration of the event. (c) Residuals of light curve approximation by four nearly equidistant peaks with parameters collected in Table 4.

resultant instrumental stellar magnitudes were then calibrated to the Johnson V photometric system by normalization to nearby stars of the Tycho-2 catalogue [23]. The light curve thus obtained (see Fig. 5) was found to agree nicely with the data of other monitoring cameras that also

Table 4. Optimal approximation parameters for the decomposition of the transient light curve into four peaks described by expression (4) and shown in Fig. 5.

T_0, c	F_0, Jy	r	d	$\Delta T, \text{s}$
18.3 ± 0.3	23.2 ± 0.6	4.0 ± 0.4	-5.4 ± 4.1	8.7 ± 0.4
27.0 ± 0.3	13.4 ± 3.4	24.8 ± 8.3	-9.7 ± 4.9	9.1 ± 0.4
36.1 ± 0.2	11.4 ± 1.7	25.9 ± 7.6	-22.0 ± 17	8.3 ± 0.5
44.4 ± 0.5	15.1 ± 1.8	21.9 ± 3.3	-5.1 ± 0.2	

Note. ΔT is the distance between a given peak and the previous one. The probability of these interpeak distances occurring at random was estimated as 10^{-3} by calculating the $\Delta T_{1,2}\Delta T_{2,3}\Delta T_{3,4}/\Delta T_{1,4}^3$ statistics from 10^5 realizations of a group of four Poisson peaks.

observed this event, like Pi of the Sky [29] and RAPTOR (RAPid Telescope for Optical Response) [30].

According to the TORTORA data, the optical radiation of the transient is confidently detected beginning from about the tenth second from the onset of the gamma-ray burst. Its intensity increases as t^4 to attain a stellar magnitude $V \approx 5.5^m$, then varies by a factor of one and a half to two on a time scale of several seconds, and finally decreases as $t^{-4.6}$, down to and below the detection threshold approximately 100 s later. In this case, the gamma-ray radiation terminates during the 57th second from the onset of the burst.

The light curve of the transient exhibits four peaks with similar amplitudes, durations, and shapes. We approximated them by a sum of four curves, each of which smoothly connects two power-law expressions describing the leading and trailing edges [31],

$$F = F_0 \left(\frac{t}{T_0} \right)^r \left(\frac{d}{d+r} + \frac{r}{d+r} \left(\frac{t}{T_0} \right)^{r+1} \right)^{-(r+d)/(r+1)}. \quad (4)$$

Here, T_0 and F_0 are the location of the peak and its integral flux, and r and d are the respective exponents for the leading and trailing edges. The parameters of these curves are collected in Table 4. The intervals between the peak maxima turn out to be almost equal, about 8.5 s, which corresponds to 4.4 s for the GRB 190308B red shift $z = 0.937$ [19]. The probability that the combination of these intervals occurs randomly is 10^{-3} (see Table 4). In the power-density spectrum of the central part of the light curve, there also exists a spike at the frequency that corresponds to the interpeak distance at a 10^{-15} significance level (Fig. 6b). Therefore, it is valid to say that we have discovered periodic variations of the transient optical emission on a time scale of a few seconds.

The power-density spectrum of gamma-ray radiation observed by the BAT detector of the Swift space telescope, which is shown in Fig. 6a, does not exhibit clearly defined features at this frequency. This might be attributed to a significant contribution of stochastic variability, which has the form of shot noise, in the frequency interval from several tens of seconds to fractions of a second [32], which may conceal a periodic structure with a moderate amplitude for a multiplicative noise character.

To analyze the variability of the light curve over short periods of time, we subtracted the smooth approximation curve with four fitted peaks from the original data and studied the residual curve shown in Fig. 5c. The Fourier analysis of its different intervals revealed indications of periodic intensity variations during the last peak, in the interval from $T = 40$ s to $T = 50$ s (see Fig. 6). The remaining phases of the light curve exhibit no signs of significant variability at frequencies

0.1–3.5 Hz (0.3–10 s) with a power exceeding 15% prior to repointing and 10% after it. To exclude the instrumental nature of these periodic intensity variations, we performed a similar analysis for comparison stars and the background flux, which revealed no similar features.

The significance level of this peak in the power-density spectrum is equal to about 1%. The period and amplitude of the corresponding sinusoidal component, derived by means of nonlinear least-square fit, are 1.13 s (0.6 s in the reference system of the burst) and 9%.

To compare the temporal structure of optical and gamma-ray light curves, we performed a cross-correlation analysis of the central part of the burst, excluding the obviously correlated regions of the intensity increase and decay [33] (Fig. 7). The correlation between the high-temporal-resolution data does not exceed 0.5 due to a significant contribution of the noise component in the 0.1–1 s range, both to the optical light curve (measurement errors) and to the gamma-ray light curve (shot-noise-like high-frequency variability of physical origin [32]). For the low-resolution data (1.3 s binning), the correlation coefficient, by contrast, amounts to 0.82 when the optical light curve is shifted 2 seconds back relative to the gamma-ray one (see Fig. 7). The correspondingly rebinned data for the gamma-ray light curve exhibit the same four peaks spaced at nearly equal intervals as the optical light curve.

The $\Delta t \approx 2$ time lag of the optical emission relative to the gamma-ray emission is a solid indication that they are generated in different parts of the burst, with the optical photons emanating from regions whose central distance is greater by $\Delta R \approx 2c\Gamma^2\Delta t(1+z)^{-1} = 1.5 \times 10^{16}\Gamma_{500}^2$ cm, where Γ_{500} is the ejected-substance Lorentz factor in units of 500 [34, 35].

The burst emission characteristics that we discovered obviously contradict the emission generation models reliant on different kinds of interaction within one ensemble of electrons and their emitted photons (synchrotron and inverse-Compton mechanisms) [19, 36, 37], the model involving two internal shock waves, forward and backward [38], and the model with relativistic turbulence in the outflow [39]. On the other hand, the steepness of the leading edges and the nearly equal durations of all four optical flares are inconsistent with the model involving an external shock, both forward and backward, as the source of the optical radiation [40].

Two models have been proposed to date that rely on internal shocks and in which optical radiation and gamma rays are generated via synchrotron mechanism in different parts of the outflow: the higher the photon energy, the closer to the central source the site of its emission is. These are the model of ‘residual collisions’ [35] and the model with a significant neutron component in the outflow [41]. In these scenarios, gamma-ray photons are emitted at the distance $10^{14} - 10^{15}$ cm from the center due to the heating of electrons at the fronts of shock waves generated in the collision of proton shells ejected from the central source. In the framework of the first model, optical photons are produced in optically thin plasma in the collision of ‘residual’ shells (the results of the merging of separate groups of initial shells) at substantially greater distances, $\gtrsim 10^{16}$ cm [35]. In the second model, the one with a significant neutron component, optical radiation is generated by the electrons emitted in the β -decay of neutrons, which reach distances $R \sim 10^{16}$ cm without interacting with other components of the outflow. The

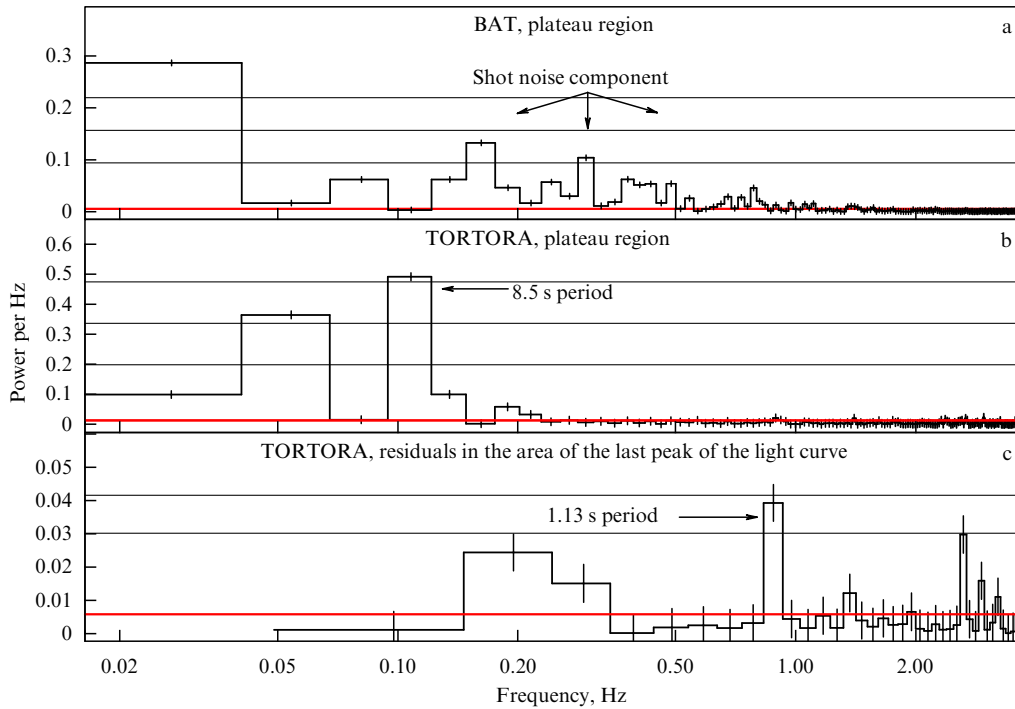


Figure 6. Power-density spectrum of the central part (from $T = 13$ s to $T = 50$ s) of the burst obtained from the data of the BAT (Burst Alert Telescope) gamma-ray telescope of the Swift spacecraft (the sum of all spectral channels) (a) and the TORTORA optical camera (b), and the power-density spectrum of the residual of the optical light curve after subtraction of the smooth approximation function, which was depicted in Fig. 5, for the interval of the last peak (from $T = 40$ s to $T = 50$ s) (c). The linear trend was subtracted from all curves. The missing part of the optical curve (the interval from $T = 24.5$ s to $T = 31$ s) with a high temporal resolution was filled with white Gaussian noise with the variance corresponding to that in the remaining part of the data and with the mean values lying on the smooth approximation curve. Errors and significance levels for the spectra were estimated by the bootstrap method, i.e., by generating a large number of synthetic light curves by randomly shuffling the intensities in the original light curve, which completely destroys its time structure but preserves the distribution of these values. The significance levels then correspond to the probability that a value exceeding the given one in any of the frequency bins randomly occurs for the power-density spectrum of a completely random process with a sampling distribution that coincides with the observed one. The feature near 9 s, which is clearly seen in the power-density spectrum of the middle part of the light curve at the significance level 10^{-15} , corresponds to the four peaks in the light curve spaced at almost equal intervals. The low-frequency components in the optical spectrum and in the gamma-ray spectrum correspond to two different intensity levels of light curves. The feature in the power-density spectrum of the difference curve with a significance level ~ 0.01 may correspond to the periodic component with the 10% amplitude and the period ≈ 1.13 s, which manifests itself during the last peak. The remaining intervals of the difference light curve do not exhibit features of this kind.

products of this decay, protons and electrons, collide with fast proton shells ejected from the central source later on, giving rise to secondary shock waves and heating the electrons, which generate synchrotron radiation. Both models explain the observed two-second lag of periodic peaks in the optical curve relative to those in the gamma-ray curve, as well as its significantly higher smoothness on the 0.1–1 s time scale in comparison with gamma-ray radiation, which exhibits high variability on this time scale [32]. On the other hand, the large quantitative difference between the optical and gamma-ray fluxes ($F_o/F_\gamma \sim 10^3$) [19] is easier to interpret in the model with the neutron component [41]. Furthermore, a significant neutron fraction in the outflow is practically inevitable in the case of bright gamma-ray bursts like GRB 080319B [42, 43]. This model is therefore preferred and our findings are strong evidence in favor of the existence of a significant neutron component in the outflow.

We note that the conclusion that the optical radiation and gamma rays are emitted at different distances from the central source directly follows from the structural similarity between the optical light curve and the gamma-ray curve, which we discovered. This conclusion is independent of both the specific mechanisms of transformation of the kinetic outflow energy to the internal energy of particles, and the particle radiation mechanisms. This effect may not stem from density

or velocity variations of substance in the outflow, like those observed in the afterglow of some other bursts on a time scale of several tens of seconds [44, 45]. It is difficult to imagine such a behavior, particularly a periodic one, which coincides in different parts of the relativistic outflow spaced by about 10^{16} cm. Therefore, we are compelled to conclude that the variations we observe have a common origin: specifically, they are caused by a periodic activity of the central source (in this case, each optical peak corresponds to one activity episode).

The discovered variability of the radiation flux from outflowed matter may be a manifestation of transient accretion caused by the periodically developing gravitational instability [46] of the hot inner parts of a massive accretion disc (about one solar mass) rotating around a black hole with a mass of three solar masses, which resulted from the collapse of the nucleus of a massive star [47, 48]. This disc must contain a substantial fraction of neutrons [43]. The four peaks seen in the optical light curve reflect four episodes of accretion activity responsible for the jet outflow of matter. The gas in the internal parts of the disc is fragmented due to various instabilities and forms separate shells inside the outflow, whose collisions generate internal shocks. Furthermore, the half-second intensity variations seen at the last stages of the burst may result from the

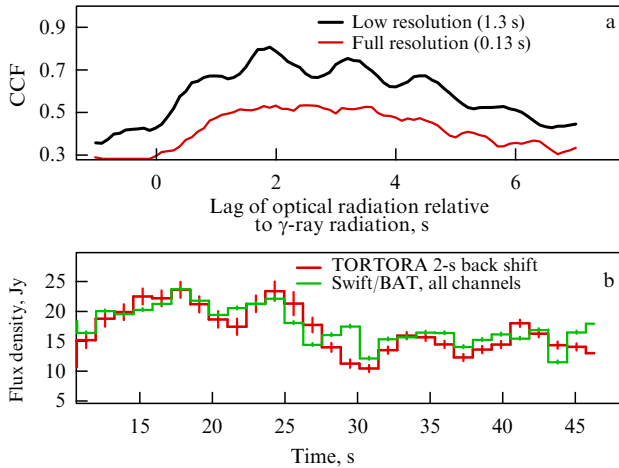


Figure 7. (a) Cross correlation (CCF) of the Swift/BAT gamma-ray curve (sum of all spectral channels) and the TORTORA optical light curve for the full (0.13 s) and low (1.3 s) temporal resolution. Only the central part of the burst was used for the analysis, with the exception of the radiation buildup and decay phases. For each value of the argument, the correlation coefficient was calculated by rebinning the gamma-ray curve, which was accordingly shifted to the optical one. The peak correlation for the high-resolution data (0.13 s) is substantially lower than for the low-resolution data (1.3 s) owing to their higher noisiness. Quasiperiodic variations of the cross correlation are due to the transition of the sharp peak of the gamma-ray curve for $T + 30$ s across the boundaries of individual bins. (b) The low-resolution light curve shifted 2 s back, and the correspondingly rebinned gamma-ray curve. In this case, the correlation coefficient r is close to 0.82 at the significance level 5×10^{-7} .

Lense–Thirring precession of the internal parts of the accretion disc.

5. Next-generation wide-field monitoring system

Obviously, it is important to further develop the methodology for the wide-field search for optical transients in two directions. First, it is required to improve the detection threshold of the system by at least 2–3 stellar magnitudes while retaining or even broadening its field of view. This may be attained with the use of multiobjective (or multitelescope) configurations by narrowing the field of view of an individual instrument and thereby improving its angular resolution [49]. The significant readout noise contribution of CCD matrices may be overcome either by improving their quantum efficiency and the gain of image intensifiers or by using low-noise electron-multiplying CCD matrices. The second important line of development is to measure the colors and polarization of the transients discovered.

In what follows, we outline one possible design of a multiobjective monitoring system based on internal-gain CCD matrices and capable of collecting multicolor and polarimetric information about transients.

5.1 Basic 3×3 unit

The proposed project has a modular structure and consists of separate base units that contain 9 objectives each and are placed on separate equatorial mounts (Fig. 8). Each objective is suspended in a gimbal controlled by two actuators and can be reoriented independently of the other ones. Furthermore, each objective has a set of color and polarization filters that may be inserted into the light beam in the course of

observation. This enables a rapid move from a filter-free wide-field monitoring to narrow-band observations, with all objectives pointing towards the same region, for instance, one containing the newly discovered transient, and observing it using all possible combinations of color and polarization filters (Fig. 9). Simultaneous observation of a transient with all objectives with the same filter is also possible in order to improve the photometric accuracy by summing their data.

Each objective is equipped with a fast electron-multiplying CCD matrix with negligible readout noise even for a high frame rate. Possible versions of mass-produced CCD matrices and objectives are depicted in Fig. 10.

The data stream from each channel of this system, which amounts to about 20 megabytes per second, is collected by a dedicated computer, which stores it on a hard disc and analyzes it in real time with the use of a method similar to that described for the FAVOR and TORTORA cameras. The operation of the system as a whole is coordinated by the dedicated computer, which receives information about the uncovered transients from individual channels and controls the change in observation regimes.

In the wide-field monitoring regime, each base unit has the field of view about 260 square degrees (720 when using Canon objectives) and the B-band detection threshold

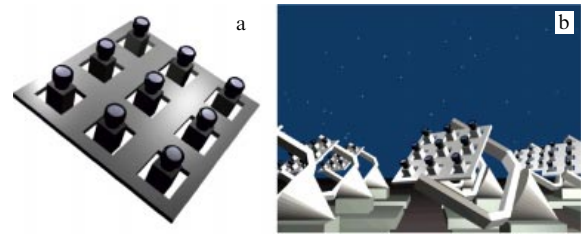


Figure 8. (a) Base 3×3 unit. Each objective is equipped with a set of installable color and polarization filters, which may be promptly inserted into the light beam and may be reoriented independently of the other ones: B, V, and R are photometric (for the B, V, and R bands) filters, and P_1 , P_2 , and P_3 are polarization filters for three different polarization orientations. (b) Artistic view of the complete monitoring system, which comprises an ensemble of base units placed on separate equatorial mountings.

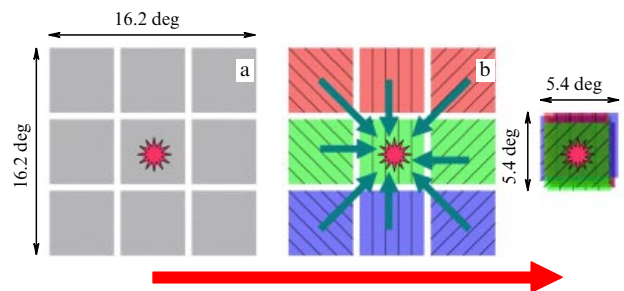


Figure 9. Different regimes of base unit operation. (a) Regime of wide-field monitoring in white light or in the transmission band of one of the color filters. (b) Insertion of color and polarization filters into the light beam as the first step following the discovery of an optical transient. (c) Repointing all objectives to the transient-containing field to simultaneously acquire information about the transient in three different photometric bands for three orientations of the polarization plane (indicated by different hatching directions). The exact time required for moving from one regime to another depends on the hardware configuration and is expected to be within 0.3 s.



Figure 10. Possible mass-produced components of the projected system: (a) Electron-multiplying Andor iXon^{EM}+888 CCD matrix with 1024×1024 pixels, each $13 \mu\text{m}$ in size; (b) Canon EF 85 f/1.2 L USM II objective capable of imaging a 9×9 degree field onto this matrix for a scale of $31''/\text{pixel}$; (c) Marshall Electronics 140 mm f/1.0 objective, which affords a 5.4×5.4 degree field for a scale of $19''/\text{pixel}$.

Table 5. Detection limits (in stellar magnitudes) of a base unit in the narrow-field regime for different combinations of photometric and polarization filters with the use of Marshall Electronics objectives. For Canon objectives, all threshold stellar magnitudes are 1.5^{m} lower.

Exposure time, s	Without filters/B	B + 3 polarizations	BVR	BVR + 3 polarizations
0.1	15.7	13.0	15.0	12.5
10	18.2	15.2	17.5	15.0
1000	20.7	17.9	20.0	17.5

$\sim 14.5^{\text{m}}$ in 0.1 s (13^{m} for Canon). Frame coaddition would increase the detection threshold up to 17^{m} for the effective exposure of 10 s and to 19.5^{m} for 1000 s (respectively to 15.5^{m} and 18^{m} with the use of Canon objectives). In the narrow-field regime, in the observation of individual objects, the field of view decreases to 30 square degrees (80 for Canon) and the detection threshold depends on the selected combination of spectral and polarization filters; these variants are summarized in Table 5. Furthermore, for bright events, the realization of a regime with high temporal resolution is possible when the CCD matrix supports the readout in a narrow window at a higher frame rate (for instance, for an Andor iXon^{EM}+888 matrix, a frame rate up to 65 Hz in the 128×128 field without binning or up to 310 Hz with an 8×8 binning is possible).

5.2 Complete system

The complete system is a set of basic units installed on separate mountings and operated in concert. Their number may be arbitrary: the greater the number is, the better the coverage of the celestial sphere and the lower the detection threshold in the narrow-field regime.

For instance, an assemblage configured of eight base units covers 2100 square degrees (5700 degrees with the use of Canon objectives) simultaneously in the sky in the wide-field monitoring regime, which allows surveying the attainable hemisphere twice per night while staying in each region for half an hour. When combining information from all 72 channels in the narrow-field regime, the detection threshold would range from 17.2^{m} to 19.7^{m} for effective exposure times from 0.1 to 10 s (the respective thresholds would be equal to 15.5^{m} and 18.2^{m} with the use of Canon objectives). The amount of data acquired by this system during a night of observations would be about 40 terabytes, which would be processed in real time as they arrive. The performance of this system in the observation of different classes of objects is shown in Figure 11 in comparison with other existing and projected wide-field monitoring systems.

Assuming that an objective costs 2 thousand euros, a CCD matrix 45 thousand euros, one computer 1 thousand euros, and a mounting 26 thousand euros, the cost of the base unit would amount to about 500 thousand euros, while the eight-unit configuration would cost about 5 million euros.

5.3 Prototype of the system

As a prototype of a multiobjective monitoring system, we are developing, with support from the Russian Foundation for Basic Research, an array consisting of nine Canon objectives with the aperture ratio 1/1.2 and the focal length 85 mm. The objectives will be equipped with a set of spectral and polarization filters, as well as with image intensifiers with GaAs photocathodes whose quantum efficiency is about 30% at the wavelength 4500 Å. The image intensifiers effectively shorten the focal length of the system by a factor of two and also permit suppressing the readout noise of fast Sony ICX285AL CCD matrices. As a result, the field of view of an individual channel is equal to about 100 square degrees (900 degrees for the complete system) for the detection threshold $B \approx 12.5^{\text{m}}$ in 0.1 s (the limiting value increases to $B \approx 15^{\text{m}}$ on summation of 100 consecutive frames, which corresponds to the effective temporal resolution of 10 s). Pointing all channels to one field permits attaining the limit $B \approx 13.5^{\text{m}}$ in 0.1 s and $B \approx 16^{\text{m}}$ in 10 s.

The prototype system will be completed and put into service in 2010–2011.

6. Conclusions

The discovery and comprehensive study of the optical companion of what is currently the brightest gamma-ray burst, GRB080319B, made using the TORTORA camera emphasizes the importance of pursuing permanent monitoring of large regions of the celestial sphere, as well as of employing detectors and techniques with high temporal resolution in the search for fast optical transients of a priori unknown localization. The FAVOR and TORTORA cameras, which were developed in the framework of the general strategy of these observations, have demonstrated the success of this strategy, allowing us to further develop this research: the next step may be the proposed new-generation wide-field monitoring system.

Acknowledgements

This work was supported by the Russian Foundation for Basic Research grant Nos. 04-02-17555, 06-02-08313, and 09-02-12053, INTAS (04-78-7366), CRDF (RP1-2394-MO-02),

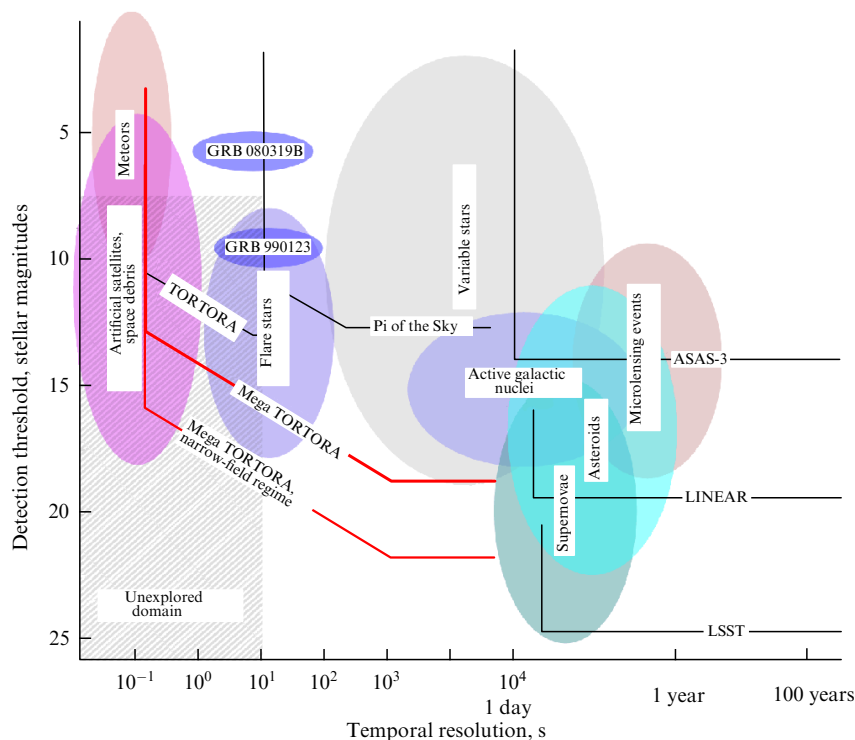


Figure 11. Efficiency of the monitoring system proposed for the observation of different classes of objects and its comparison with the efficiency of other instruments, such as the presently operating facilities (ASAS-3 (All sky Automated Survey), LINEAR (Lincoln Near-Earth Asteroid Research), Pi of the Sky, FAVOR/TORTORA), and those planned for the future [LSST (Large Synoptic Survey Telescope)].

the Progetti Pluriennali 2003 Grant of Bologna University, the Program of the Presidium of the Russian Academy of Sciences, and a grant from the President of the Russian Federation for the Support of Young Russian Scientists.

References

1. Bondi H Q. *J. R. Astron. Soc.* **11** 443 (1970)
2. Schaefer B E *Astron. J.* **90** 1363 (1985)
3. Schaefer B E et al. *Astron. Astrophys.* **174** 338 (1987)
4. Tamagawa T et al. *Nuovo Cimento C* **28** 771 (2005)
5. Borozdin K N et al. *Proc. SPIE* **4847** 344 (2002)
6. Castro-Tirado A J et al. *Astron. Astrophys. Suppl.* **138** 583 (1999)
7. Burd A et al. *New Astron.* **10** 409 (2005)
8. Shvartsman V F et al. *Pis'ma Astron. Zh.* **14** 233 (1988) [*Sov. Astron. Lett.* **14** 97 (1988)]
9. McBreen S et al. *Astron. Astrophys.* **380** L31 (2001)
10. Afanasiev V L, Kalenichenko V V, Karachentsev I D *Astrofiz. Byull.* **62** 319 (2007) [*Astrophys. Bull.* **62** 301 (2007)]
11. Beskin G M et al. *Astron. Astrophys. Suppl.* **138** 589 (1999)
12. Eichler D, Beskin G *Astrobiology* **1** 489 (2001)
13. Zolotukhin I et al. *Astron. Nachrichten* **325** 675 (2004)
14. Karpov S et al. *Nuovo Cimento C* **28** 747 (2005)
15. Molinari E et al. *Nuovo Cimento B* **121** 1525 (2006)
16. Zerbi F M et al., in *Gamma-ray Bursts in the Afterglow Era* (ESO Astrophys. Symp., Eds E Costa, F Frontera, J Hjorth) (Berlin: Springer-Verlag, 2001) p. 434
17. Beskin G et al. *Nuovo Cimento C* **28** 751 (2005)
18. Karpov S et al. *GRB Coordinates Network Circular* (7452) 1 (2008)
19. Racusin J L et al. *Nature* **455** 183 (2008)
20. Beskin G et al., arXiv:0905.4431
21. American department of defense satellite ephemerides database, <http://www.spacetrack.org/>
22. Bertin E, Arnouts S *Astron. Astrophys. Suppl.* **117** 393 (1996)
23. Høg E et al. *Astron. Astrophys.* **355** L27 (2000)
24. Barthelmy S D *AIP Conf. Proc.* **428** 129 (1998)
25. Guarnieri A et al. *GRB Coordinates Network Circular* (5372) 1 (2006)
26. Karpov S et al. *GRB Coordinates Network Circular* (5897) 1 (2006)
27. Karpov S et al. *GRB Coordinates Network Circular* (5941) 1 (2006)
28. Racusin J L et al. *GRB Coordinates Network Circular* (7427) 1 (2008)
29. Cwiok M et al. *GRB Coordinates Network Circular* (7439) 1 (2008)
30. Wozniak P et al. *GRB Coordinates Network Circular* (7464) 1 (2008)
31. Kocovski D, Ryde F, Liang E *Astrophys. J.* **596** 389 (2003)
32. Margutti R et al. *AIP Conf. Proc.* **1065** 259 (2008)
33. Beskin G et al. *AIP Conf. Proc.* **1065** 251 (2008)
34. Piran T *Rev. Mod. Phys.* **76** 1143 (2005)
35. Li Z, Waxman E *Astrophys. J.* **674** L65 (2008)
36. Kumar P, Panaitescu A *Mon. Not. R. Astron. Soc.* **391** L19 (2008)
37. Fan Y-Z, Piran T *Frontiers Phys. China* **3** 306 (2008)
38. Yu Y W, Wang X Y, Dai Z G *Astrophys. J.* **692** 1662 (2009)
39. Narayan R, Kumar P *Mon. Not. R. Astron. Soc.* **394** L117 (2009)
40. Zou Y-C, Piran T, Sari R *Astrophys. J. Lett.* **692** L92 (2009)
41. Fan Y-Z, Zhang B, Wei D-M *Phys. Rev. D* **79** 021301(R) (2009)
42. Derishev E V, Kocharovskiy V V, Kocharovskiy V I *Astrophys. J.* **521** 640 (1999)
43. Pruet J, Woosley S E, Hoffman R D *Astrophys. J.* **586** 1254 (2003)
44. Jakobsson P et al. *New Astron.* **9** 435 (2004)
45. Bersier D et al. *Astrophys. J. Lett.* **584** L43 (2003)
46. Masada Y et al. *Astrophys. J.* **663** 437 (2007)
47. Woosley S E *Astrophys. J.* **405** 273 (1993)
48. Zhang W, Woosley S E, Heger A *Astrophys. J.* **608** 365 (2004)
49. Beskin G et al. *Bull. Special Astrophys. Observatory* **60–61** 217 (2007)